The Solution Structure of a Cardiac Troponin C−Troponin I−Troponin T Complex Shows a Somewhat Compact Troponin C Interacting with an Extended Troponin I−Troponin T Component†

William T. Heller,‡ Ekram Abusamhadneh,§ Natosha Finley,§ Paul R. Rosevear,§ and Jill Trewhella*,‡

Bioscience Division, Los Alamos National Laboratory, Los Alamos, New Mexico 87545, and Department of Molecular Genetics, Biochemistry and Microbiology, College of Medicine, University of Cincinnati, Cincinnati, Ohio 45267

Received August 20, 2002; Revised Manuscript Received October 22, 2002

ABSTRACT: We have investigated the structure of the cTnC−cTnI−cTnT(198−298) calcium-saturated, ternary cardiac troponin complex by small-angle scattering with contrast variation. Shape restoration was also applied to the scattering information resulting from the deuterated cTnC subunit, the unlabeled cTnI−cTnT(198−298) subunits, and the entire complex. The experimental results and modeling indicate that cTnC adopts a partially collapsed conformation, while the cTnI−cTnT(198−298) components have an extended, rod-like structure. Shape restoration applied to the X-ray scattering data and the entire contrast variation series suggest that cTnC and the cTnI−cTnT(198−298) component lie with their long axes roughly parallel to one another with a relatively small surface area for interaction. Our findings indicate that the nature of the interactions between TnC and the TnI−TnT component differs significantly between the cardiac and skeletal isoforms as evidenced by the different degrees of compactness between the cardiac TnC and skeletal TnC in their respective ternary complexes and the fact that the cTnC subunit is not highly intertwined with the other subunits, as observed in the binary complex of the skeletal isoforms [Olah, G. A., and Trewhella, J. (1994) *Biochemistry 33*, 12800−12806].

In the sliding-filament model of striated muscle action, thick and thin filaments move past each other to accomplish contraction or relaxation. The thick filaments are composed of myosin, while the thin filaments are a double-stranded helical assembly of actin monomers with tropomyosin polymerized head to tail in the grooves of the actin helix (covering approximately seven actin monomers). Each tropomyosin is bound to one troponin. The contractile force is generated by the cyclic attachment and detachment of the myosin S1 heads to the actin monomers whereby a power stroke, driven by actin−S1 myosin ATPase activity, occurs some time during the attachment phase of the cycle (for reviews, see refs *1*−*4*). Troponin and tropomyosin form a Ca^{2+}-sensitive switch that regulates this cycle of attachment and detachment.

Troponin is composed of three subunits. TnC[1] binds Ca^{2+}; TnI inhibits the attachment of myosin or actin in the absence of the Ca^{2+} signal, and TnT anchors troponin to the thin filament and plays a role in transmitting the Ca^{2+} signal along the thin filament. Two isoforms of TnC and TnI exist in striated muscle: slow skeletal or cardiac (cTnC and cTnI) and fast skeletal (sTnC and sTnI). The isoforms show important structural and functional differences. In the case of TnI, the cardiac isoform has a 32-residue N-terminal extension with two adjacent serine residues (positions 23 and 24) that can be phosphorylated by PKA in response to β-adrenergic stimulation (*5*). The phosphorylation event is believed to alter conformational equilibria within the regulatory domain of cTnC, thereby changing the Ca^{2+} sensitivity of the complex (*6*).

Crystallography and NMR reveal that isolated sTnC and cTnC have two globular lobes separated by a flexible linker that forms an extended helix of seven or eight turns in the crystal structure (*7*−*13*). Pairs of helix−loop−helix Ca^{2+}-binding domains make up each globular lobe, which overall has a "cup" shape; the sides of the cup are formed by pairs of helices with the calcium-binding loops as the base. The Ca^{2+} affinity of the C-terminal "structural" domain of sTnC, which is always occupied in muscle, differs from that of the N-terminal "regulatory" domain by 2 orders of magnitude (*14*). The differences in the binding affinities of the two domains in cTnC are comparable, but the N-terminal Ca^{2+}-binding site I is inactive (*15*). Ca^{2+} binding to the regulatory

† This work was performed under the auspices of the U.S. Department of Energy (Contract W-7405-ENG-36) and was supported by National Institutes of Health Grants GM40528 (J.T.) and AR44324 (P.R.R.) and DOE/BER Project KP110101 (J.T.) in support of the Oak Ridge Structural Molecular Biology Center. Neutron scattering data were obtained using instrumentation supported by the National Science Foundation under agreement DMR-9423101 at the Cold Neutron Research Facility at the National Institute of Standards and Technology.

* To whom correspondence should be addressed. Phone: (505) 667-2690. Fax: (505) 667-2670. E-mail: jtrewhella@lanl.gov.

‡ Los Alamos National Laboratory.

§ University of Cincinnati.

[1] Abbreviations: TnC, troponin C; TnI, troponin I; TnT, troponin T; cTnC, recombinant rat cardiac troponin C (des-Met[1]-Ala[2], Cys35Ser); cTnI, recombinant mouse cardiac troponin I; cTnT(198−298), residues 198−298 of recombinant rat cardiac troponin T; sTnC, skeletal troponin C; sTnI, skeletal troponin I; sTnT, skeletal troponin T; NMR, nuclear magnetic resonance; FRET, fluorescence resonance energy transfer; R_g, radius of gyration; d_{max}, maximum linear dimension; AEBSF, 4-(2-aminoethyl)benzenesulfonyl fluoride hydrochloride; BME, β-mercaptoethanol; PMSF, phenylmethanesulfonyl fluoride; DTT, dithiothreitol; PKA, cAMP-dependent protein kinase A.

10.1021/bi026687c CCC: $22.00
Published on Web 12/06/2002

domain of sTnC produces a conformational change such that the cup-shaped domain opens, leading to an increase in the accessible hydrophobic surface area (*12*, *16*). In the case of cTnC, the opening of the regulatory domain requires both Ca^{2+} and a cTnI peptide sequence to be present (*17*, *18*). The opening of the regulatory domain changes the TnC−TnI interaction such that the inhibition of the actin−myosin interaction by TnI is eliminated.

Unlike TnC, there are no high-resolution structure coordinates available for the other subunits, although a preliminary crystal structure of a ternary complex was recently described (*19*). Crystallography and NMR studies of TnC interacting with peptide fragments of TnI and TnT provide details of local interactions (*17*, *20*−*33*), while NMR studies of the binary cTnC−cTnI complex indicate that the C-terminal domain of cTnC interacts with the N-terminal domain of cTnI in an antiparallel manner (*34*). This mode of interaction is also suggested by studies using cTnI peptide fragments (*35*, *36*).

Neutron scattering with selective deuterium labeling has been employed to map out the shapes and dispositions of the individual subunits within fast skeletal troponin complexes. Our contrast variation study of the Ca^{2+}-saturated sTnC−sTnI binary complex (*37*) revealed that both subunits are highly extended. The sTnC structure is similar to the sTnC crystal structure (*7*) except the N-terminal regulatory domain is in a more open configuration consistent with it being Ca^{2+}-loaded and interacting with sTnI. The sTnI adopts an extended spiral structure that wraps around the sTnC, passing through the hydrophobic cleft in the N-terminal lobe and near that in the C-terminal lobe (*38*). The dimensions of the sTnI spiral are consistent with it being largely α-helical. In a subsequent modeling study constrained by several sources of experimental data, we presented a high-resolution model for the binary complex that also predicted an unusual extended *β*-hairpin structure for the inhibitory sequence segment of sTnI (*39*). This putative actin-binding motif is observed in the crystal structure of the actin−profilin complex (*40*).

Stone et al. (*41*) used neutron scattering, solvent matching, and selective deuteration with reconstituted troponin to evaluate the component structures in the ternary, skeletal troponin complex. Their study also found that sTnC is in an extended conformation consistent with the crystal structure of sTnC (*7*). Further, sTnC did not undergo a measurable conformation change upon removal of Ca^{2+}. The sTnI structure in the ternary complex was more extended than sTnC, but it is more compact than what we observed in the binary complex, possibly due to additional interactions involving sTnT.

We present here a combined X-ray and neutron small-angle scattering study with contrast variation of the Ca^{2+}-saturated cTnC−cTnI−cTnT(198−298) complex formed using deuterated cTnC. This particular complex is stable, highly soluble, and monodisperse in solution. We have been able to determine the low-resolution shapes and relative dispositions of the cTnC and cTnI−cTnT(198−298) components in the ternary complex. The results show that there are important differences between the cardiac and skeletal troponin complexes. In particular, the cTnC component adopts a somewhat compact shape, though not as compact as that observed for sTnC interacting with amphipathic helical peptides (*42*), nor as compact as calmodulin in complex with peptides (for reviews, see refs *43* and *44*). The results also indicate that cTnC and cTnI are not highly intertwined as they are in sTnC and sTnI in the binary complex (*37*−*39*).

MATERIALS AND METHODS

Troponin Complex Formation. [^{15}N,D]cTnC and cTnI were expressed and purified as previously described (*6*). cDNA encoding cTnT(198−298) was generated by PCR and subcloned into the pET23d$^+$ expression vector. cTnT(198−298) was expressed in BL21(DE3)-RIL cells and purified by chromatography on Pharmacia CM-Sepharose and Superdex 75 columns. Complex formation was carried out by dissolving cTnC, cTnI, and cTnT(198−298) at a molar ratio of 1:1:1.1 in 6 M urea, 150 mM NaCl, 25 mM Tris (pH 7.5), 1 mM EDTA, 1 mM DTT, and 1 mM PMSF. An extensive dialysis against 25 mM Tris (pH 7.5), 10 mM BME, 10 mM DTT, 10 mM $CaCl_2$, 0.1 mM AEBSF, and 0.1 mM leupeptin followed. Complex formation was monitored by following individual [^{15}N,D]cTnC amide resonances in H−^{15}N HSQC NMR spectra. NMR samples of the Ca^{2+}-saturated [^{15}N,D]cTnC−cTnI−cTnT(198−298) complex (0.4−1.0 mM) were prepared by exchanging the [^{15}N,D]cTnC−cTnI−cTnT(198−298) complex into buffer containing 10% D_2O, 20 mM Tris-d_{11} (pH 6.8), 500 mM KCl, 10 mM $CaCl_2$, 5 mM DTT, 5 mM BME, 0.1 mM AEBSF, and 0.1 mM leupeptin. If necessary, the [^{15}N,D]cTnC−cTnI−cTnT(198−298) complex was further purified by size exclusion chromatography on a Pharmacia Superdex 75 column equilibrated in 20 mM Tris (pH 7.5), 500 mM KCl, 10 mM $CaCl_2$, 5 mM BME, and 1 mM PMSF.

Preparation of Stock Solutions. Stock solutions of the cTnC−cTnI−cTnT(198−298) complex were prepared in H_2O and D_2O buffers for use in both the X-ray and neutron scattering measurements. The H_2O and D_2O buffers contained 425 mM KCl, 10 mM $CaCl_2$, 0.1 mM AEBSF, 0.1 mM leupeptin, 1 mM PMSF, 20 mM Tris, 5 mM BME, and 5 mM DTT. Stock solutions were titrated using either HCl or DCl to a final pH of 7.2. Equal amounts of the original cTnC−cTnI−cTnT(198−298) sample (∼4.5 mg/mL) were allowed to dialyze against the H_2O and D_2O buffers for 16 h. The dialysis membrane had an 8 kDa molecular mass cutoff. Fractions of both dialysis buffers were retained for background measurements in the scattering experiments.

Small-Angle X-ray Scattering Measurements. Small-angle X-ray scattering measurements were performed with the two instruments at Los Alamos National Laboratory. The measurements served to evaluate the samples for nonspecific aggregation and the influence of interparticle interference, as well as provide a data set for the contrast variation series. The first instrument generates a line source (*9*), while the second produces a focused, point source (*45*). The monodispersity of the sample was characterized using the line source instrument by collecting data at a series of protein concentrations. Measurements were made at relative fractional concentrations (*c*) of 1.0, 0.8, 0.6, 0.4, and 0.2 of the complex in the H_2O and D_2O stock solutions. Additionally, data were collected for a lysozyme standard (*46*) at the same fractional concentrations to calibrate the $I(0)$ values for determining protein concentrations. Data reduction followed

published procedures to correct for detector sensitivity and background signal (*9*). The point source instrument was used to collect the X-ray scattering data used in the structural analysis and contrast variation series because it produces significantly higher quality data with minimal instrumental "smearing" due to the finite dimensions of the X-ray source. Measurements were taken on the complex in H_2O. To minimize radiation damage to the sample, five data sets were collected with a fresh sample for 3 h each. Data reduction followed published procedures (*44*). The five data sets were averaged to improve the signal to noise in the data to be included in the contrast variation series.

Small-Angle Neutron Scattering Measurements. Mixtures of the H_2O and D_2O stock sample solutions were made with 0, 15, 57.5, 80, and 100% of the D_2O stock solution in preparation for measuring five different neutron contrast values. Corresponding background solutions were mixed by weight to achieve optimal background subtraction for the samples in the neutron scattering data analysis. The actual hydrogen content of the stock D_2O buffer solution was determined using NMR (data not shown) with fully deuterated tetrahydrofuran as the standard. The hydrogen content was found to be ~16% and was likely due to the high water content in the buffer salts. The results of the hydrogen content determination were used throughout the analysis of the data, but the percentage mixtures for the H_2O/D_2O solutions are given as unadjusted numbers representing the mixing of the stock solutions.

Small-angle neutron scattering experiments were performed at the National Institute for Standards and Technology Center for Neutron Research (Gaithersburg, MD) using the NG-3 30m SANS instrument (*47*). The neutron wavelength was set to 5.5 Å with a wavelength spread $\Delta\lambda/\lambda$ of 0.34 to maximize the neutron flux. Sample and background intensities were collected for all five contrasts at detector distances of 2.5 and 6 m. Data reduction followed standard procedures (*47*) to correct for detector sensitivity and sample background. The data sets from the two distances were merged using the routines included with the data reduction software.

Small-Angle Scattering Data Analysis. The scattering of X-rays or neutrons from monodisperse particles in a homogeneous solution has the form

$$I(q) = |\langle \int_V [\rho(\vec{r}) - \rho_s] e^{-i\vec{q}\cdot\vec{r}} d^3r \rangle|^2 \qquad (1)$$

where $\rho(\vec{r})$ is the scattering length density of the scattering particle and ρ_s is the scattering length density of the solvent. $\vec{\mathbf{q}}$ is the momentum transfer, having the magnitude $4\pi(\sin\theta)/\lambda$, where 2θ is the scattering angle and λ is the wavelength. The integration over the particle volume is rotationally averaged, and the experiment measures the time and ensemble average for all particles in solution.

In addition to traditional Guinier analysis of the data for R_g (*48*), small-angle scattering data can be analyzed for the probable distribution of vector lengths within the scattering object $P(r)$. $I(q)$ and $P(r)$ are related by the Fourier transform in eq 2.

$$I(q) = 4\pi \int_0^\infty dr\, P(r) \sin(qr)/(qr) \qquad (2)$$

The indirect Fourier transform algorithm developed by Moore (*49*) was used to determine $P(r)$ from the measured intensity. The approach uses an expansion in $(\sin(qr))/qr$ to fit the intensity profiles. The boundary conditions $P(r)/r = 0$ at $r = 0$ and d_{max} are applied to $P(r)$.

Contrast variation is a powerful tool for studying proteins in solution. The dramatic difference in the scattering lengths of hydrogen and deuterium makes it possible to change the scattering length density of a protein by substituting one isotope for the other. Small-angle neutron scattering data for a sample composed of two components with different isotope labeling patterns are collected in several H_2O/D_2O mixtures. The contrast series of measurements provides intensity profiles $I(q)$ that can be written as a set of linear equations in the basic scattering functions corresponding to the scattering functions of the deuterated and nondeuterated components and a cross term (*37*). A multiple linear regression routine (*50*) was implemented in the C programming language at Los Alamos National Laboratory to solve for the three basic scattering functions that are then used to derive information about the shapes of the components, as well as their disposition.

Shape Restoration. Shape restoration is an attempt to determine the three-dimensional shape of a scattering particle from the one-dimensional intensity profile. Shape restoration was applied to the X-ray scattering intensity profile and to the basic scattering functions extracted from the contrast variation data in an effort to develop structural models of the ternary complex, the cTnC component, and the cTnI−cTnT(198−298) components. Shape restoration was accomplished using the program GA_STRUCT, which produces models of the shape of the scattering object using aggregates of spheres. The approach is similar to that of Chacón et al. (*51*, *52*). However, the spheres are not constrained to lie on a grid; they may have arbitrary radii, and the intensity calculation that is employed is a Monte Carlo integration technique that has been used previously by this group (*9*, *37*, *53*, *54*). GA_STRUCT differs from previous implementations in that it generates a family of several *ab initio* models that fit the data. The members of the family are then characterized for similarity to produce a consensus envelope representing the structure that is consistent across the majority of the models in the family. The quality of the fit of the model intensities to the data is evaluated using the least-squares fitting parameter given in eq 3.

$$F = \frac{1}{N_{pts}} \left\{ \sum_{N_{pts}} \frac{[I(q) - I_m(q)]^2}{\sigma(q)^2} \right\} \qquad (3)$$

F is similar to the reduced χ^2 value, but it does not take into account the number of degrees of freedom used. $I(q)$ and $I_m(q)$ are the experimental and model intensities, respectively. $\sigma(q)$ is the experimental uncertainty in the measured intensity. N_{pts} is the number of data points. Models were generated of the cTnC and cTnI−cTnT(198−298) components from the basic scattering functions. Additionally, GA_STRUCT was employed to produce a model of the ternary complex from the small-angle X-ray scattering data. A family of 25 models was produced for each intensity profile to generate each consensus envelope. Multiple restorations were performed with GA_STRUCT to ensure the reproducibility of the resulting structures.

To determine the relative position and orientation of the cTnC and cTnI−cTnT(198−298) components in the complex, models of the ternary complex were produced using the two consensus envelopes generated from the basic scattering functions and the intensity profiles of the complete contrast variation series. The model of the complex was produced with software developed at Los Alamos National Laboratory called CONTRAST. The program generates composite models from a set of known structures. The known structures can be either atomic coordinates, such as a crystal structure, or shapes, such as a consensus envelope from GA_STRUCT. Composite model structures are made by randomly positioning and orienting the known structures with respect to one another. The contrasts of each component, which are determined from the chemical composition of the scattering particle and solvent, are used to calculate each intensity in the contrast variation series for each random configuration. In calculating $P(r)$, the program assumes that the scattering length density for each component structure is uniform. $I(q)$ is determined by calculating the Fourier transform of $P(r)$ (eq 2). The quality of the fit of the model intensity profiles to each intensity profile in the contrast variation series is measured using F (eq 3) summed over all intensity profiles in the series. CONTRAST has the ability to normalize the density of the composite structure for models where the volumes of the components overlap. The components, which are required to have the same density, are said to have overlapping volumes when points within one component lie within a user-specified distance of more than four points of the other component. To normalize the density of points in the final structure, points from one component are removed if they are found to lie within the other model according to the above criterion. The model intensity profiles are calculated using only the remaining points.

In addition to modeling the cTnC−cTnI−cTnT(198−298) complex, CONTRAST was used to generate a model of cTnC in the ternary complex from an atomic-resolution NMR structure of cTnC in the binary complex (*55*). The basic scattering function of cTnC was used as the target intensity profile. To provide flexibility in generating a model from the NMR structure, it was divided into three parts. Break points were inserted into the cTnC sequence after Cys^{84} and Gly^{91} for generating the model. The component structures were allowed to have arbitrary rotations about the break points but were constrained to remain linked together.

RESULTS

Structural Parameters from Small-Angle Scattering

To prepare samples for neutron scattering, troponin complex formation was followed by monitoring cTnC H and ^{15}N amide resonances in two-dimensional H−^{15}N HSQC NMR spectra. Several amide resonances show unique chemical shifts for cTnC free in solution, bound to cTnI, and bound to the cTnI−cTnT(198−298) component. Gel filtration chromatography was used to remove any excess troponin proteins and provide an estimate of the troponin complex molecular weight consistent with a 1:1:1 stoichiometry. Densitometric analysis of the ratios of Coomassie blue-stained cardiac troponin subunits, separated by SDS−polyacrylamide gel electrophoresis, showed that the ratio of the troponin subunits is identical within the accuracy of the method.

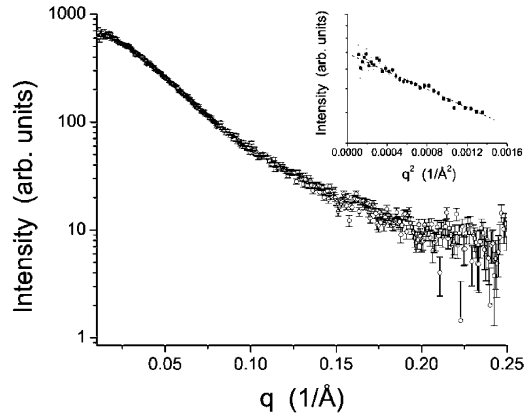

FIGURE 1: Small-angle X-ray scattering intensity profile resulting from the point source instrument. The intensity profile is the average of five data sets. The inset graph is a Guinier plot {log[$I(q)$] vs q^2} (*48*) of the low-q region of the data. The dashed line is a linear fit to the data.

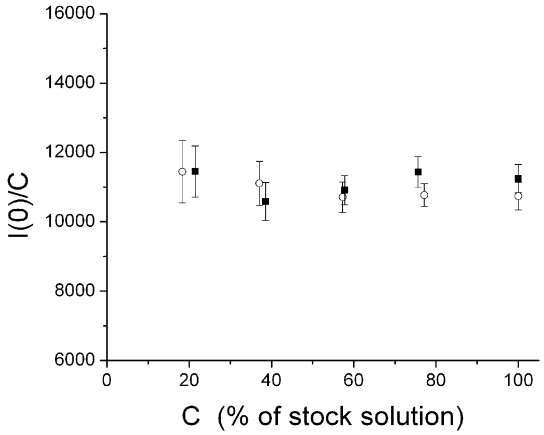

FIGURE 2: $I(0)/c$ plotted as a function of the relative concentration. The concentration series collected for H_2O (○) and D_2O (■) demonstrate that the forward scatter of the samples is independent of concentration.

The results of the small-angle X-ray scattering measurements performed with the point-source instrument at Los Alamos National Laboratory are shown in Figure 1. The Guinier region of the data is a straight line (inset). The small-angle X-ray scattering data resulting from the instrument with the line source served as a check of the sample quality. Guinier plots showed a linear region consistent with a particle in solution having a single R_g. In addition, the $I(0)/c$ versus c data (Figure 2) for the H_2O and D_2O samples show no concentration dependence and no evidence of D_2O-induced aggregation. It can be concluded that the samples are monodisperse, identically shaped particles and there are no concentration dependent interparticle interference effects that would bias the structural parameters derived from the scattering data. The $I(0)$ values were used to determine the concentration of the complex by comparison with a lysozyme standard (*46*) and using the relation $I_{lys}(0)/m_{lys}c_{lys} = I_{tn}(0)/m_{tn}c_{tn}$, where lys stands for lysozyme, tn stands for troponin, m is the molecular weight, and c is the concentration in milligrams per milliliter. The protein concentrations of the H_2O and D_2O stock solutions were 4.7 and 5.5 mg/mL, respectively.

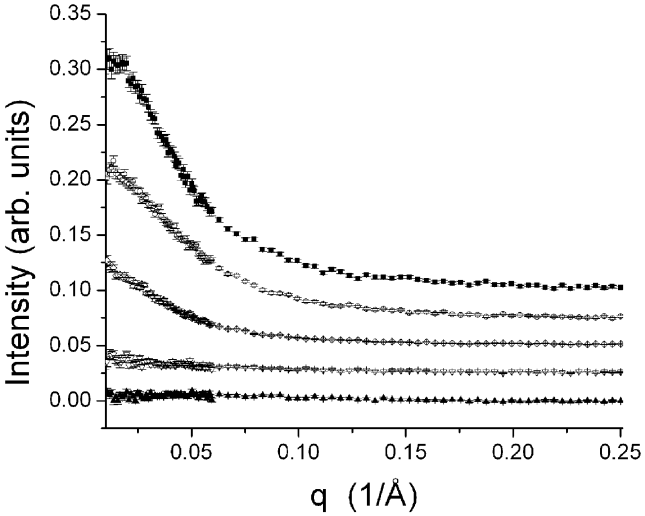

FIGURE 3: Contrast variation series collected on the NG3-SANS instrument at the National Institute of Standards and Technology (*47*) in 0 (■), 15 (○), 57.5 (▲), 80 (▽), and 100% D_2O buffer (◇). The curves are offset for clarity. The change in data quality at ~0.065 $Å^{-1}$ results from the use of two detector distances. The two distances were required to collect data over a *q* range sufficiently broad to ensure that accurate structural parameters could be extracted from the data.

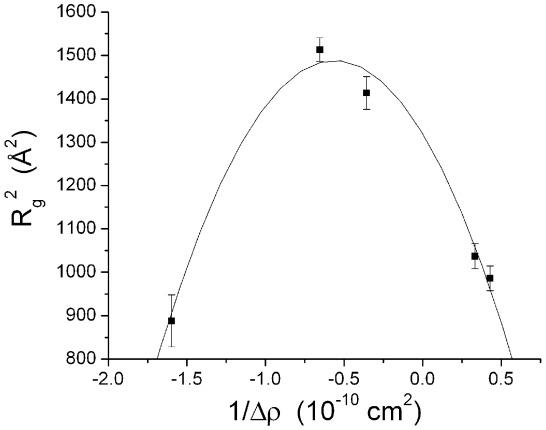

FIGURE 4: Stuhrmann plot (R_g^2 vs $1/\Delta\rho$) of the contrast variation series (*37*, *56*). The data point from the 57.5% D_2O solution was omitted because of the low signal to noise in the data. The solid line is a second-degree polynomial fit to the data.

The small-angle neutron scattering intensities collected for the contrast variation series are shown in Figure 3. The entire series has been normalized for the path length of the sample cell. The neutron and X-ray scattering data were binned to improve the signal to noise and give intensity profiles with even and equal sampling. R_g was determined from each contrast variation point to produce a Stuhrmann plot (*56*; also see ref *37* for the implementation used here), shown in Figure 4. Stuhrmann analysis relates the R_g as a function of the contrast of the complex to the R_g of the subunits and the separation of the centers of mass through a quadratic form. The curvature is directly and independently related to the curvature of a second-degree polynomial fit to the data. The curve has a clear quadratic character, indicating that the centers of mass of the cTnC and cTnI−cTnT(198−298) components are not coincident. Analysis of the curvature indicates that the centers of mass are separated by approximately 46 ± 3 Å.

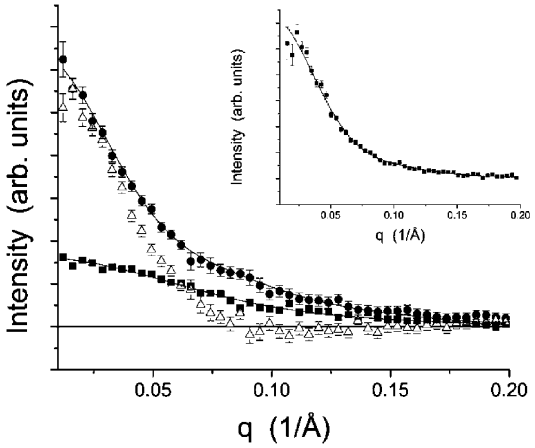

FIGURE 5: Basic scattering functions plotted as a function of *q* in the main plot. The intensity profiles for cTnC (■) and the cTnI−cTnT(198−298) component (●) are plotted with a sample curve from the shape restoration by GA_STRUCT to show the quality of fit to the data obtained by the *ab initio* method. The cross term (△), corresponding to the scattering between the two components, is also included. The inset shows the rebinned X-ray scattering data with a representative curve from the shape restoration by GA_STRUCT to show the quality of the fit to the data.

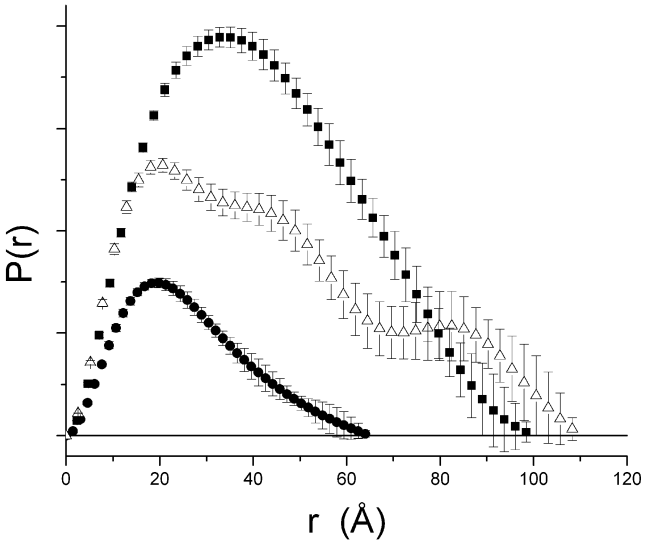

FIGURE 6: Distance distribution functions *P*(*r*) calculated from the basic scattering functions [cTnC (●) and cTnI−cTnT(198−298) (△)] and X-ray scattering data (■). The area under the curves has been normalized to the molecular weights.

The basic scattering functions of the deuterated cTnC and the nondeuterated cTnI−cTnT(198−298) components extracted from the entire contrast series (five neutron sets and the X-ray data) are shown in the main plot of Figure 5 with the cross term. The corresponding *P*(*r*) functions of the two components are shown in Figure 6 along with the *P*(*r*) derived from the X-ray scattering data, which reflects the shape of the entire complex. The areas under the curves are normalized to the respective molecular weights. Table 1 summarizes the R_g and d_{max} values determined from the X-ray scattering data from the complex and the basic scattering functions of the components. Other published structural parameters for cardiac and skeletal troponin components are included in Table 1 for comparison. The *P*(*r*) of the complex indicates it has an asymmetric shape, as do the two components [cTnC and cTnI−cTnT(198−298)]. The R_g and

Table 1: Structural Parameters of the Troponin Complex and Isotopically Labeled Components As Determined by $P(r)$ Analysis Using the Moore Algorithm (*49*)[a]

	R_g (Å)	d_{max} (Å)
cTnC−cTnI−cTnT(198−298)	33.1 ± 0.5	100 ± 5
cTnC	20.1 ± 0.7	65 ± 5
cTnI−cTnT(198−298)	35.0 ± 1.4	115 ± 8
$2Ca^{2+}$−sTnC (*7*)	23.9	72
$2Mg^{2+}$−sTnC (*9*)	23.0 ± 0.2	70 ± 3
$4Ca^{2+}$−sTnC in complex with sTnI(1−47) (*27*)	18.4	63
$4Ca^{2+}$−sTnC in a binary complex (*37*)	23.9 ± 0.5	72 ± 3
$4Ca^{2+}$−sTnC in a ternary complex (*41*)	24.1 ± 0.2	−
sTnI in a binary complex (*37*)	41.2 ± 2.0	118 ± 4
sTnI in a ternary complex (*41*)	33.0 ± 2.0	−
sTnC−sTnI (*31*)	33.0 ± 0.5	115 ± 4

[a] Structural parameters determined for the crystal structure of sTnC and the subunits of the sTn complexes derived from neutron scattering (*37*, *41*) are provided for comparison.

Table 2: Structural Parameters of the Consensus Envelopes (env.) and the Average Volume of the Individual Models (ave.) Produced by GA_STRUCT from the Basic Scattering Functions and the X-ray Scattering Data[a]

	R_g (Å)	d_{max} (Å)	V (Å^3)	F
TnC−TnI−TnT(198−298)	33.0	112	97200 (env.) 119000 (ave.) (67800)	1.06−1.10
TnC	21.4	68	41400 (env.) 36100 (ave.) (22700)	1.307−1.310
TnI−TnT(198−298)	36.5	118	69200 (env.) 73800 (ave.) (44400)	0.46−0.57

[a] The volumes in parentheses are the expected volumes based on the molecular weights of the proteins.

d_{max} derived from the cTnC basic scattering function indicate that it has a compact structure that is intermediate to the fully extended form observed for sTnC in the ternary complex (*41*) and the "collapsed" sTnC structure observed in its complex with melittin (*42*). The cTnI−cTnT(198−298) component has a rod-like, extended shape. The d_{max} values of the complex and of the cTnI−cTnT(198−298) component are consistent to within error. Calculating the first moment of the $P(r)$ from the cross term provides a measure of the distance between the centers of mass of the two components. This calculation yields a distance of 48.8 ± 0.3 Å, which is consistent with the Stuhrmann analysis.

Modeling

GA_STRUCT successfully produced consensus envelopes from the basic scattering functions and the X-ray scattering data. The resulting models fit the data well, with the F values being shown in Table 2. The fits of representative model intensity profiles to the basic scattering functions and the X-ray scattering data produced by GA_STRUCT are shown in Figure 5. Table 2 also summarizes the R_g, d_{max}, and volume determined for the consensus envelopes. The expected volume calculated from the molecular weight is included for comparison.

cTnC Component. The fit to the data obtained by GA_STRUCT, as estimated by the F value, is very good. Three orthogonal views of the cTnC consensus envelope, which is reproduced in multiple runs of GA_STRUCT, are shown in Figure 7A. The structure is peanut-shaped, suggesting that there is some separation of the two lobes of the protein. The maximum linear dimension of the envelope is consistent with that determined from the $P(r)$ analysis, while the width of the envelope is ∼32 Å. The volume of the envelope is ∼82% higher than expected on the basis of the molecular weight of the protein, while the average volume of the individual models is ∼59% larger than the expected value. These inflated volumes can in part be attributed to the low-resolution nature of the data that results in models in which the surfaces will tend to be smoothed. It also appears that the grid-based algorithm used to generate the consensus envelope further inflates the volume. The inflated volume also may reflect some inherent flexibility in the structure. Small-angle scattering samples a time- and ensemble-averaged solution structure. As a result, the protein density for a flexible structure effectively smears out over a larger volume than one would expect for a static structure. Tests of our modeling method using small-angle scattering intensities calculated from more globular and rigid crystal structures find that the general shape of the consensus envelope agrees very well with the original structure. The R_g, d_{max}, and volume are also reproduced by the consensus envelope (data available on request). Shape restoration was also performed by DAMIN (*57*) on the cTnC basic scattering function (not shown). The overall length of the DAMIN model agrees with our consensus envelope; however, the structure is narrower than our consensus envelope, and the end lobes of the structure are smaller than the Ca^{2+}-binding domains of cTnC.

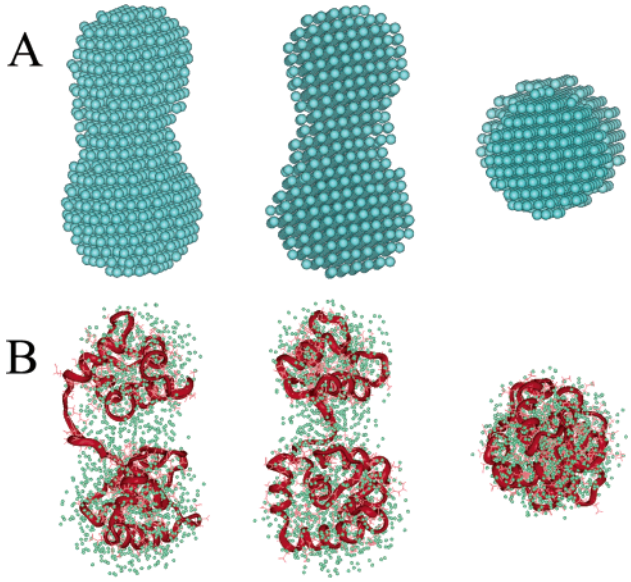

FIGURE 7: Consensus envelope produced by GA_STRUCT from the cTnC basic scattering function shown in three orthogonal views in panel A. The high-resolution structure produced by CONTRAST is shown in panel B as a ribbon representation in red. The high-resolution structure is docked onto the consensus envelope from panel A (the small green spheres) in a representation that allows both structures to be seen. The structures shown in Figures 8, 9, and 11 are to scale with those shown here.

Three orthogonal views of the high-resolution model of cTnC produced from the NMR structure and CONTRAST are shown overlaid onto the GA_STRUCT consensus envelope in Figure 7B. The F value of the model is 1.43. The left and center images confirm that the consensus

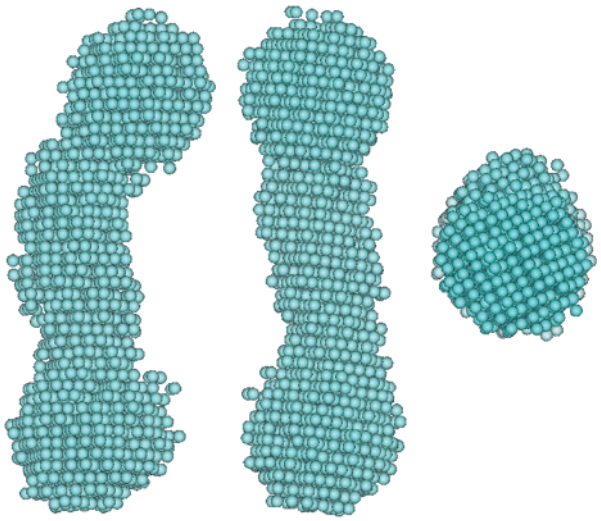

FIGURE 8: Consensus envelope produced by GA_STRUCT for the cTnI−cTnT(198−298) basic scattering function shown in three orthogonal views.

envelope has a larger volume than the protein. The bulk of the volume difference is in the linker region between the two globular domains in the consensus envelope, which is the region that has been identified as showing flexibility in the uncomplexed cTnC (*58*). The length and width of the two models are in excellent agreement. The high-resolution structure determined by CONTRAST cannot be expected to be biochemically accurate. However, the results clearly demonstrate that a partially collapsed cTnC with flexibility in the interconnecting helix agrees with the scattering data and the particle envelope produced by GA_STRUCT from the basic scattering function.

cTnI−cTnT(198−298) Component. Three orthogonal views of the consensus envelope are shown in Figure 8. The particle is more extended than cTnC, with subtle hints of the structure having a long, helical pitch reminiscent of the structure of sTnI complexed with sTnC (*38*). The longest dimension is consistent with the $P(r)$ analysis, while the width is 25−30 Å. The volume of the consensus envelope is ∼55% larger than that expected from the molecular weight. In contrast to the results for cTnC, the average volume for the individual models is just slightly larger than the consensus envelope, perhaps indicating a less flexible structure.

cTnC−cTnI−cTnT(198−298) Complex. The particle envelope produced from the X-ray scattering data by GA_STRUCT is shown in three orthogonal views in Figure 9. The d_{max} of the envelope is consistent with the $P(r)$ of the X-ray data and the d_{max} of the cTnI−cTnT(198−298) component. Inspection of the envelope suggests that cTnC binds at a position slightly offset from the center of the cTnI−cTnT(198−298) component. The width of the end lobe of the long segment is ∼40 Å, similar to that of the cTnI−cTnT(198−298) component. The volume is 43% larger than expected from the molecular weight of the complex.

CONTRAST was used to generate models of the ternary complex from the two basic scattering function envelopes and all the contrast variation series data. Two independent runs of CONTRAST were performed that placed different overlap restrictions on the envelopes, as described in Materials and Methods. The fitting parameter evaluated for the entire contrast series for the final model was 2.37 for

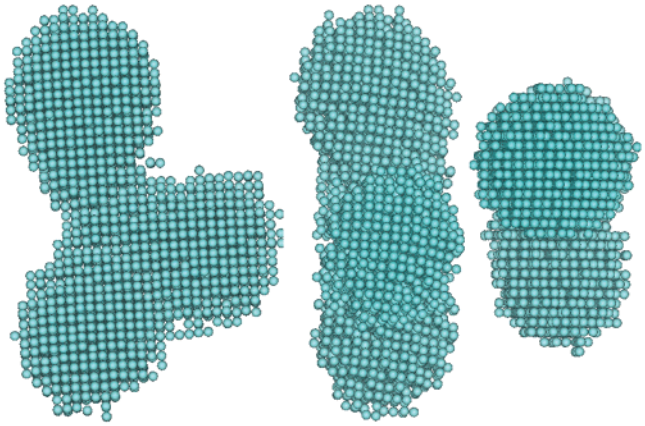

FIGURE 9: Consensus envelope produced by GA_STRUCT from the X-ray scattering data from the cTnC−cTnI−cTnT(198−298) complex shown in three orthogonal views.

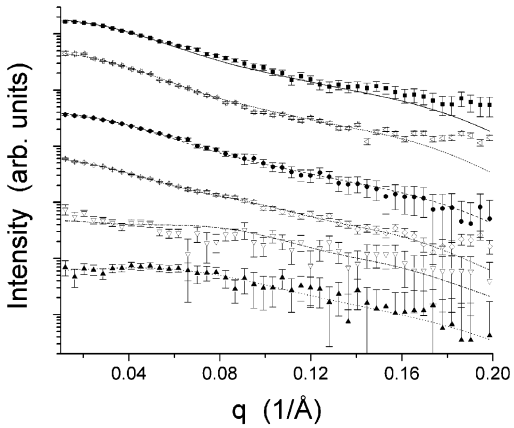

FIGURE 10: Fit of the model intensity profiles from the shape restoration by CONTRAST of the complex using the basic scattering function consensus envelopes to the contrast variation series data. All six intensity profiles are shown: 0 (■, —), 15 (●, − − −), 57.5 (▲, ···), 80 (▽, −·−), and 100% D_2O (◇, −··−) and the X-ray scattering data (triangle pointing to the left, - - -). The curves are offset for clarity. The deviation between the model and data is greatest for the 0% D_2O data.

both runs of CONTRAST. The fit of the set of model intensities to the contrast variation data that resulted from the case where the overlapping volume between the D and H components was attributed to cTnC is shown in Figure 10. This model was selected over the model resulting from the second run of CONTRAST (not shown), in which the overlapping volume was attributed to the cTnI−cTnT(198−298) component, because this approach resulted in a cTnC molecule that was too small. Our best fit model is in good agreement with the contrast series data, except for the deviations in the 0% D_2O data at high q values. Hydrogen causes significant incoherent neutron scattering that has the potential to introduce errors in the background subtraction for this data set that would impact the high-q data. Three orthogonal views of the model produced by CONTRAST are shown in Figure 11. One end of the cTnC is in contact with one end of the cTnI−cTnT(198−298) component. It extends back toward the center of the cTnI−cTnT(198−298) component at an angle. The distance between the centers of mass is ∼45 Å, which agrees with the Stuhrmann plot and the first moment of the cross term. The d_{max} of the particle remains consistent with that from the analysis of the X-ray

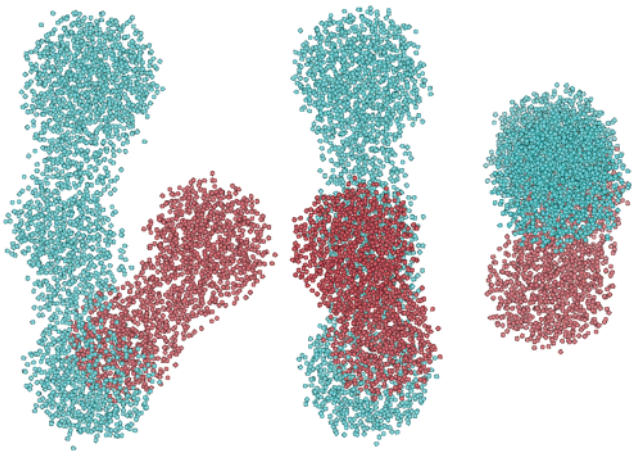

FIGURE 11: Three orthogonal views of the model of the ternary complex produced by CONTRAST using the consensus envelopes generated from the basic scattering functions. The cTnC subunit is red, and the cTnI−cTnT(198−298) component is green.

scattering data, being that of the cTnI−cTnT(198−298) component. As can be seen, the structures generated by GA_STRUCT from the X-ray scattering data and by CONTRAST using the entire contrast variation series are similar.

CONCLUSIONS

In this paper, we have developed the first model of the ternary cardiac troponin complex that shows the low-resolution structures of cTnC and the cTnI−cTnT(198−298) components and their relative dispositions within the troponin complex. Our model provides important insight into the differences between the cardiac and skeletal isoforms of troponin. In the ternary cTn complex, the cTnC subunit adopts a partially collapsed conformation wherein the two lobes of the molecule are closer together than in the crystal structure, but not in contact. The results also suggest that the interaction between cTnC and the cTnI−cTnT(198−298) component is limited to a relatively small surface area, indicating that the structures are not highly intertwined like the binary sTnC−sTnI complex (*37*−*39*). The majority of studies of cardiac troponin involve the study of interactions between fragments cTnC and cTnI, focusing on those implicated in the regulation of the contractile cycle in response to the Ca^{2+} signal and the influence of phosphorylation of Ser^{23} and Ser^{24} of cTnI (*29*, *59*−*61*). Such studies provide little or no information about the interactions between the intact proteins or regarding the role of cTnT in the complex. A preliminary crystal structure for the ternary cTn complex has been presented in which the cTnI−cTnT(198−298) components are extended helices with the cTnC located near one end (*19*). The authors have suggested, however, that there are significant crystal packing forces influencing the structure of the highly flexible cTnI and cTnT. Our model provides important information regarding the relationship between the subunits within the complex when it is in solution that will aid in the interpretation of higher resolution structural information.

The solution structures of the isolated globular domains of cTnC have been determined by NMR [PDB entry 1AJ4 (*58*)]. The NMR study found the central helix to be unstructured and flexible (*58*), which would give rise to an ensemble of solution structures having a range of R_g and d_{max} values. Other NMR studies have also shown the central helix to be flexible (*62*−*64*). NMR has also been used to determine the solution structure of Ca^{2+}-saturated cTnC bound to cTnI [PDB entry 1LA0 (*55*)]. The model of cTnC produced by CONTRAST (Figure 7B) provides an indication of the distribution of mass within the particle that is consistent with the R_g and d_{max} determined from the scattering data. Our studies do not provide unambiguous information about the relative orientation of the N- and C-domains, but our neutron scattering work provides good constraints on the distance between the domains. Interestingly, the separation and orientation of the domains for our model (Figure 7B) are consistent with the NMR study of cTnC in the binary complex. FRET measurements of the interdomain distance within cTnC have been performed for the free protein (*65*, *66*) and when it is bound in the ternary complex (*66*). The mean distance between site III and Cys^{35} in cTnC was determined to be ∼48 Å when in complex with cTnI or the cTnI−cTnT component regardless of whether a cation was bound at site II (*66*). This distance is consistent with a cTnC structure in the ternary complex derived from our basic scattering function (Figure 7B).

A more collapsed state has been observed for sTnC in the crystal structure of its complex with sTnI(1−47) (*27*). In this case, the two lobes of sTnC are in contact such that the sTnI(1−47) peptide forms contacts with both the N- and C-domains of sTnC. The weak nature of the interactions between the sTnI(1−47) peptide and the N-domain suggests that the compact nature of sTnC may be a consequence of the crystallization. The evolutionarily related, multipurpose protein calmodulin exhibits similar behavior when bound to peptides (*53*, *67*, *68*), but the details of the interaction and the degree of compaction differ. The calcium-binding domains of calmodulin have hydrophobic patches that are turned toward each other when the protein is bound around a peptide. In contrast, the hydrophobic patches in the sTnC−sTnI(1−47) complex are oriented such that they are on opposite sides of the molecular surface (*27*). Recently, the relative orientation of the calcium-saturated cTnC domains bound to a cTnI peptide was investigated using H−^{15}N residual dipolar couplings (*55*). The relative spatial orientations of the cTnC domains were calculated utilizing a rigid body molecular dynamics protocol from the results and previously determined long-range distance constraints. The d_{max} of ∼73 Å for cTnC bound to cTnI was constrained by the experimentally determined R_g for the sTnC−sTnI complex (*37*, *38*) and an interdomain FRET distance (*66*). In the resulting cTnC structure, the hydrophobic clefts face each other as if they are clamping the cTnI peptide (*55*). The crystal and solution structures show similar bending between the domains of 90° and 70°, respectively. The azimuth and twist about the bends differ such that the orientation of the hydrophobic clefts differs significantly.

Neutron scattering studies of the ternary skeletal troponin complex by Stone and co-workers (*41*) indicate sTnC retains an extended conformation (Table 2) in both the presence and absence of Ca^{2+}, consistent with the crystal structure of free Ca^{2+}-loaded sTnC (*8*). The ∼17% smaller R_g value we determined for cTnC in the ternary cardiac complex is significant. The model presented in Figure 7B demonstrates that it is possible to collapse cTnC in a manner consistent

with our measurements. At the present time, the differences in the conformation of the two isoforms of TnC in the troponin complex are not completely understood in terms of the differences in function. It appears that the interaction between the troponin components gives rise to significantly different conformations for both TnC and its partners in the complex. Conformational differences observed in the regulatory domains of cTnC and sTnC are also likely to result from an alteration in the equilibria between the "open" and "closed" states of the EF hands. Lack of an active Ca^{2+} binding site I in cTnC may decrease the stability of the open conformation, thereby increasing the extent of dissociation of Ca^{2+} from site II (*69*).

Differences in the TnT constructs between the different experiments should also be considered when attempting to reconcile observed R_g values for TnC isoforms. X-ray and neutron scattering studies on sTn utilized the TnT-T3 skeletal isoform (*41*). In contrast, the cTnT(198−298) N-terminal truncation was utilized in these studies, which resulted in reconstituted complexes with greater solubility than intact cTnT and a decreased tendency to aggregate with time. Truncation of the N-terminus also decreases the total molecular mass of the complex, which facilitates NMR studies of the ternary cTn complex. Electron microscopy and three-dimensional reconstruction of troponin on the thin filament suggests that troponin density appears as a narrow stalk, corresponding to a portion of TnT and a bulb comprising the remainder of the complex (*70*). Correlation of three-dimensional reconstructions with molecular shape information about the individual troponin proteins obtained from these scattering experiments in combination with higher-resolution NMR studies of individual proteins in the troponin complex will ultimately lead to new insights into the molecular basis for muscle contraction.

ACKNOWLEDGMENT

We thank Dr. Jürgen Schmidt of the Bioscience Division of Los Alamos National Laboratory for his assistance in performing the NMR calibration of the hydrogen content of the neutron scattering samples. We thank Dr. Jamie Schulz for assistance with the neutron scattering data acquisition and reduction at the National Institute of Standards and Technology.

SUPPORTING INFORMATION AVAILABLE

Results of modeling the basic scattering functions and X-ray scattering data with GA_STRUCT, including the structures of the individual models, as well as the consensus envelopes. This material is available free of charge via the Internet at http://pubs.acs.org.

REFERENCES

1. Holmes, K. C. (1997) *Curr. Biol. 7*, R112−R118.
2. Cook, R. (1997) *Physiol. Rev. 77*, 671−697.
3. Gergely, J. (1998) *Adv. Exp. Med. Biol. 453*, 169−176.
4. Perry, S. V. (1999) *Mol. Cell. Biochem. 190*, 9−32.
5. Moir, A. J., Solaro, R. J., and Perry, S. V. (1980) *Biochem. J. 185*, 505−513.
6. Abbott, M. B., Dong, W. J., Dvoretsky, A., DaGue, B., Caprioli, R. M., Cheung, H. C., and Rosevear, P. R. (2001) *Biochemistry 40*, 5992−6001.
7. Herzberg, O., and James, M. N. G. (1985) *Nature 313*, 653−659.
8. Sundaralingam, M., Bergstrom, R., Strasburg, G., Rao, S. T., Roychowdhury, P., Greaser, M., and Wang, B. C. (1985) *Science 227*, 945−948.
9. Heidorn, D. B., and Trewhella, J. (1988) *Biochemistry 27*, 909−915.
10. Hubbard, S. R., Hodgson, K. O., and Doniach, S. (1988) *J. Biol. Chem. 263*, 4151−4158.
11. Slupsky, C. M., and Sykes, B. D. (1995) *Biochemistry 34*, 15953−15964.
12. Gagné, S. M., Tsuda, S., Li, M. X., Smillie, L. B., and Sykes, B. D. (1995) *Nat. Struct. Biol. 2*, 784−789.
13. Houdusse, A., Love, M. L., Dominquez, R., Grabarek, Z., and Cohen, C. (1997) *Structure 5*, 1695−1711.
14. Potter and Gergely (1975) *J. Biol. Chem. 250*, 4628−4633.
15. Van Eerd, J. P., and Takahashi, K. (1975) *Biochem. Biophys. Res. Commun. 64*, 122−127.
16. Herzberg, O., Moult, J., and James, M. N. G. (1986) *J. Biol. Chem. 261*, 2638−2644.
17. Li, M. X., Spyracopoulos, L., and Sykes, B. D. (1999) *Biochemistry 38*, 8289−8298.
18. Dong, W.-J., Xing, J., Villain, M., Hellinger, M., Robinson, J. M., Chandra, M., Solaro, R. J., Umeda, P. K., and Cheung, H. C. (1999) *J. Biol. Chem. 274*, 31382−31390.
19. Takeda, S., Yamashita, A., Maeda, K., and Maeda, Y. (2002) *Biophys. J. 82*, 170A.
20. Ngai, S.-M., Sonnichson, F. D., and Hodges, R. S. (1994) *J. Biol. Chem. 269*, 2165−2172.
21. Pearlstone, J. R., and Smillie, L. B. (1995) *Biochemistry 34*, 6932−6940.
22. Tripet, B. P., Van Eyk, J. E., and Hodges, R. S. (1997) *J. Mol. Biol. 271*, 728−750.
23. McKay, R. T., Tripet, B. P., Hodges, R. S., and Sykes, B. D. (1997) *J. Biol. Chem. 272*, 28494−28500.
24. McKay, R. T., Pearlstone, J. R., Corson, D. C., Gagné, S. M., Smillie, L. B., and Sykes, B. D. (1998) *Biochemistry 37*, 12419−12430.
25. McKay, R. T., Tripet, B. P., Pearlstone, J. R., Smillie, L. B., and Sykes, B. D. (1999) *Biochemistry 38*, 5478−5489.
26. Li, M. X., Spyracopoulos, L., and Sykes, B. D. (1998) *Biophys. J. 74*, A51.
27. Vassylyev, D. G., Takeda, S., Wakatsuki, S., Maeda, K., and Maeda, Y. (1998) *Proc. Natl. Acad. Sci. U.S.A. 95*, 4847−4852.
28. Finley, N., Abbott, M. B., Abusamhadneh, E., Gaponenko, V., Dong, W., Gasmi-Seabrook, G., Howarth, J. W., Rance, M., Solaro, R. J., Cheung, H. C., and Rosevear, P. R. (1999) *FEBS Lett. 453*, 107−112.
29. Gasmi-Seabrook, G. M., Howarth, J. W., Finley, N., Abusamhadneh, E., Gaponenko, V., Brito, R. M., Solaro, R. J., and Rosevear, P. R. (1999) *Biochemistry 38*, 8313−8322.
30. Gasmi-Seabrook, G. M., Howarth, J. W., Finley, N., Abusamhadneh, E., Gaponenko, V., Brito, R. M., Solaro, R. J., and Rosevear, P. R. (1999) *Biochemistry 38*, 14432−14432.
31. Hernández, G., Blumenthal, D. K., Kennedy, M. A., Unkefer, C. J., and Trewhella, J. (1999) *Biochemistry 38*, 6911−6917.
32. Mercier, P., Li, M. X., and Sykes, B. D. (2000) *Biochemistry 39*, 2902−2911.
33. Mercier, P., Spyracopoulos, L., and Sykes, B. D. (2001) *Biochemistry 40*, 10063−10077.
34. Krudy, G. A., Kleerhoper, Q., Guo, X., Howarth, J. W., Solaro, R. J., and Rosevear, P. R. (1994) *J. Biol. Chem. 269*, 23731−23735.
35. Sheng, Z., Pan, B.-S., Miller, T. E., and Potter, J. D. (1992) *J. Biol. Chem. 267*, 25407−25413.
36. Farah, C. S., Miyamoto, C. A., Ramos, C. H. I., deSilva, A. C. R., Quaggio, R. B., Fujimori, K., Smillie, L. B., and Reinach, F. C. (1994) *J. Biol. Chem. 269*, 5230−5240.
37. Olah, G. A., Rokop, S. E., Wang, C.-L. A., Blechner, S. L., and Trewhella, J. (1994) *Biochemistry 33*, 8233−8239.
38. Olah, G. A., and Trewhella, J. (1994) *Biochemistry 33*, 12800−12806.
39. Tung, C. S., Wall, M. E., Gallagher, S. E., and Trewhella, J. (2000) *Protein Sci. 9*, 1312−1326.
40. Schutt, C. E., Myslik, J. C., Rozycki, M. D., Goonesekere, N. C. W., and Lindberg, U. (1995) *Nature 365*, 810−816.
41. Stone, D. B., Timmins, P. A., Schneider, D. K., Krylova, I., Ramos, C. H. I., Reinach, F. C., and Mendelson, R. A. (1998) *J. Mol. Biol. 281*, 689−704.
42. Blechner, S. L., Olah, G. A., Strynadka, N. C. J., Hodges, R. S., and Trewhella, J. (1992) *Biochemistry 31*, 11326−11334.

43. Ikura, M. (1996) *Trends Biochem. Sci. 21*, 14−17.
44. Chin, D., and Means, A. R. (2000) *Trends Cell Biol. 10*, 322−328.
45. Gallagher, S. C., Callaghan, A. J., Zhao, J., Dalton, H., and Trewhella, J. (1999) *Biochemistry 38*, 6752−6760.
46. Krigbaum, W. R., and Kugler, F. R. (1970) *Biochemistry 9*, 1216−1223.
47. Hammouda, B., Barker, J. G., and Krueger, S. (1996) *Small-Angle Neutron Scattering Manuals*, National Institute of Standards and Technology, Gaithersburg, MD.
48. Guinier, A. (1939) *Ann. Phys. (Paris) 12*, 161−237.
49. Moore, P. B. (1980) *J. Appl. Crystallogr. 13*, 168−175.
50. Bevington, P. R. (1969) *Data Reduction and Error Analysis for the Physical Sciences*, McGraw-Hill, New York.
51. Chacón, P., Morán, F., Díaz, J. F., Pantos, E., and Andreu, J. M. (1998) *Biophys. J. 74*, 2760−2775.
52. Chacón, P., Morán, F., Díaz, J. F., and Andreu, J. M. (2001) *J. Mol. Biol. 299*, 1289−1302.
53. Krueger, J. K., Bishop, N. A., Blumenthal, D. K., Zhi, G., Beckingham, D., Stull, J. T., and Trewhella, J. (1998) *Biochemistry 37*, 17810−17817.
54. Zhao, J., Hoye, E., Boylan, S., Walsh, D. A., and Trewhella, J. (1998) *J. Biol. Chem. 273*, 30448−30459.
55. Dvoretsky, A., Abusamhadneh, E., Howarth, J., and Rosevear, P. R. (2002) *J. Biol. Chem.* (in press).
56. Ibel, K., and Stuhrmann, H. B. (1975) *J. Mol. Biol. 93*, 255−265.
57. Svergun, D. I. (1999) *Biophys. J. 76*, 2879−2886.
58. Sia, S. K., Li, M. X., Spyracopoulos, L., Gagné, S. M., Liu, W., Putkey, J. A., and Sykes, B. D. (1997) *J. Biol. Chem. 272*, 18216−18221.
59. Dong, W.-J., Chandra, M., Xing, J., Solaro, R. J., and Cheung, H. C. (1997) *Biochemistry 36*, 6745−6753.
60. Dong, W.-J., Chandra, M., Xing, J., She, M., Solaro, R. J., and Cheung, H. C. (1997) *Biochemistry 36*, 6754−6761.
61. Reiffert, S. U., Jaquet, K., Heilmeyer, L. M. G., Jr., and Herberg, F. W. (1998) *Biochemistry 37*, 13516−13525.
62. Kleerekoper, Q., Howarth, J. W., Guo, X., Solaro, R. J., and Rosevear, P. R. (1995) *Biochemistry 34*, 13343−13352.
63. Abbott, M. B., Gaponenko, V., Abusamhadneh, E., Finley, N., Li, G., Dvoretsky, A., Rance, M., Solaro, R. J., and Rosevear, P. R. (2000) *J. Biol. Chem. 275*, 20610−20617.
64. Abbott, M. B., Dong, W.-J., Dvoretsky, A., DaGue, B., Capriolo, R. M., Cheung, H. C., and Rosevear, P. R. (2001) *Biochemistry 40*, 5992−6001.
65. Wang, C.-L. A., and Leavis, P. C. (1990) *Arch. Biochem. Biophys. 276*, 236−241.
66. Dong, W.-J., Robinson, J. M., Xing, J., Umeda, P. K., and Cheung, H. C. (2000) *Protein Sci. 9*, 280−289.
67. Krueger, J. K., Olah, G. A., Rokop, S. E., Zhi, G., Stull, J. T., and Trewhella, J. (1997) *Biochemistry 36*, 6017−6023.
68. Krueger, J. K., Gallagher, S. C., Zhi, G., Geguchadze, R., Persechini, A., Stull, J. T., and Trewhella, J. (2001) *J. Biol. Chem. 276*, 4535−4538.
69. Pääkkönen, K., Annila, A., Sorsa, T., Pollesello, P., Tilgmann, C., Kilpeläinen, I., Karisola, P., Ulmanen, I., and Drakenberg, T. (1998) *J. Biol. Chem. 273*, 15633−15638.
70. Lehman, W., Rosol, M., Tobacman, L. S., and Craig, R. (2001) *J. Mol. Biol. 307*, 739−744.

BI026687C